Degradation Mechanisms of C_6/$LiNi_{0.5}Mn_{0.3}Co_{0.2}O_2$ Li-ion Batteries Unraveled by Non-destructive and Post-mortem Methods

Dongjiang Li[a,b], Hu Li[a], Dmitri L. Danilov[b,c], Lu Gao[c], Xiaoxuan Chen[a], Zhongru Zhang[a],

Jiang Zhou[d], Rüdiger-A. Eichel[b,e], Yong Yang[a,*] and Peter H. L. Notten[b,c,f,*]

[a] College of Chemistry and Chemical Engineering, Xiamen University, Xiamen, 361005, China

[b] Forschungszentrum Jülich, Fundamental Electrochemistry (IEK-9), D-52425 Jülich, Germany

[c] Eindhoven University of Technology, Eindhoven, 5600 MB, The Netherlands

[d] Tianjin Lishen Battery Joint-stock Co., Ltd., Tianjin, 300384, China

[e] RWTH Aachen University, D-52074 Aachen, Germany

[f] University of Technology Sydney, Broadway, Sydney, NSW 2007, Australia

* Corresponding authors:

Peter H. L. Notten and Yong Yang

Email address: p.h.l.notten@tue.nl (Peter Notten) and yyang@xmu.edu.cn (Yong Yang)

Abstract

The ageing mechanisms of $C_6/LiNi_{0.5}Mn_{0.3}Co_{0.2}O_2$ batteries at various discharging currents and temperatures have systematically been investigated with electrochemical and post-mortem analyses. The irreversible capacity losses (ΔQ_{ir}) at various ageing conditions are calculated on the basis of regularly determined electromotive force (EMF) curves. Two stages can be distinguished for the degradation of the storage capacity at 30°C. The first stage includes SEI formation, cathode dissolution, *etc*. The second stage is related to battery polarization. The various degradation mechanisms of the individual electrodes have been distinguished by $dV_{EMF}/dQ\ vs\ Q_{out}$ and $dV_{EMF}/dQ\ vs\ V$ plots. The Solid-Electrolyte-Interface (SEI) formation as well as the electrode degradation has been experimentally confirmed by XPS analyses. Both Ni and Mn elements are detected at the anode while Co is absent, indicating that the bonding of Co atoms is more robust in the cathode host structure. A Cathode-Electrolyte-Interface (CEI) layer is also detected at the cathode surface. The composition of the CEI layer includes Li salts, such as LiF, LiCOOR, as well as transition metal compounds like NiF_2. Cathode dissolution is considered to be responsible for both the NiF_2 detected at the cathode and Ni at the anode.

Introduction

The ternary nickel-manganese-cobalt (NMC) electrode system has drawn significant attention in the recent development of commercial Li-ion batteries due to their larger specific energy densities compared to LiFePO$_4$ and lower cost compared to LiCoO$_2$ [1]. With the different ratios of the transition metals, many compounds, such as LiNi$_{1/3}$Co$_{1/3}$Mn$_{1/3}$O$_2$ (NMC(111)), LiNi$_{0.5}$Co$_{0.2}$Mn$_{0.3}$O$_2$ (NMC(532)), LiNi$_{0.6}$Co$_{0.2}$Mn$_{0.2}$O$_2$ (NMC(622)), LiNi$_{0.8}$Co$_{0.1}$Mn$_{0.1}$O$_2$ (NMC(811)) *etc.*, have been successfully synthesized. All these compounds have a layered structure, consisting of Ni^{2+}, Mn^{4+} and Co^{3+} in the as-made materials, according to the electronic structure studies [2-5]. Ni^{2+} will be oxidized to Ni^{4+} during the initial stages of charging, while Co^{3+} will be oxidized to Co^{4+} at higher voltage ranges. Mn^{4+} remains inactive throughout normal charging [5, 6] and provides structural stability [7]. The electrode specific capacity increases therefore with increasing Ni content in the compound. Consequently, only NMC(111), NMC(532) and NMC(622) have up till now been widely applied as cathode materials in commercial Li-ion batteries.

Graphite is commonly used as anode in most Li-ion batteries due to the excellent cycling performance, high safety and considerable specific capacity. Generally, Li immobilization in the Solid-Electrolyte-Interface (SEI) layers is considered to be the main degradation mechanism at graphite electrodes [8-13]. The SEI growth consumes cyclable Li ions, leading to irreversible capacity losses. Although the graphite electrode is considered as a stable anode material, structural degradation has also been reported under severe ageing conditions [14-17]. Transition metal deposition [16, 17] and diffusion-induced-stress (DIS) [18, 19] are considered responsible for graphite degradation.

The degradation mechanism of NMC, on the other hand, is still under discussion. Transition metal dissolution is generally accepted as common feature of NMC in LiPF$_6$-based acidic solutions, especially at elevated temperatures [20, 21]. The dissolved metal ions can be precipitated at the anode, damaging the SEI structure and leading to higher battery capacity losses. The NMC material can also experience structural transformation during ageing, *e.g.* a phase transition from the rhombohedral space group $R\bar{3}m$ to the monoclinic space group C2/m when the charge voltage is beyond 4.4 V *vs* Li$^+$/Li [5, 22-24]. Li-Ni site interchange is considered to be another detrimental effect on the electrode cycling performance [7, 22-26]. Due to the similar ionic radius of Ni^{2+} (0.67 Å) and Li$^+$ (0.76 Å), there is always a possibility that these two ions exchange their crystallographic sites, consequently, inducing local disorder in NMC materials. The fixed Ni ions in the Li layers will then block the Li diffusion pathways, leading to a significant decrease of the cathode rate capability.

In the present work the aging mechanisms of NMC(532) batteries will be investigated with electrochemical measurements and postmortem chemical analyses. The irreversible capacity losses, which are obtained from the EMF curves at various discharging currents and temperatures, will be discussed. Furthermore, the various degradation mechanisms of the individual electrodes can be identified by a newly proposed non-destructive method: EMF voltage derivative analyses [15-17]. Finally, the growth of the SEI layer at the anode and the CEI layer at the cathode will be investigated by X-ray photoelectron spectroscopy (XPS).

2. Experimental

2.1 *Cycle life testing*

For the cycling experiments a set of commercial 2.5 Ah cylindrical NMC (ANR18650) batteries (LG Co., Ltd.) has been selected. The electrochemical experiments were carried out with automatic cycling equipment (Neware). The batteries, subjected to the cycling experiments, were kept in climate chambers in order to control the temperature at 30, 45 and 60ºC.

Before conducting the cycling experiments all batteries were activated during 5 cycles and the subsequent characterization cycles were also carried out at 30, 45 and 60ºC, corresponding to the cycling temperatures, to obtain the electromotive force (EMF) curves. During characterization all batteries were charged in the constant-current constant-voltage (CCCV) mode. A 0.5 C charging rate was used in the CC-mode followed by CV charging at 4.2 V during 1 hour. The batteries were then discharged at various constant currents (0.1, 0.2, 0.3, 0.5 and 1.0 C-rate) in the subsequent cycles, using a cut-off voltage of 3.0 V. On the basis of these sets of discharge curves, the EMF was extracted by mathematical extrapolation.

After the characterization process has been completed all batteries were cycled under various conditions, which are summarized in Table 1. The second column shows the various discharging currents and the last column the duration of each cycle. The charging current of all cycling experiments is fixed at 0.5 C. There is always a resting period of 20 min after the (dis)charging step. Since the cycling time of each cycle is strongly dependent on the current, the duration of each cycle varies in different experiments. Note that the actual duration of each cycle for a given discharge current is also varying due to the decreasing battery capacity upon cycling, as indicated by the duration ranges in Table 1. All batteries were regularly re-characterized after approximately every 20 days.

Table 1. Cycling conditions for NMC batteries.

	Temperature			Duration of each
	30ºC	45ºC	60ºC	cycle (hours)
Discharging	0.1	0.1	0.1	13.2~7.5
current	0.5	0.5	0.5	5.6~3.2
(C-rate)	1.0	1.0	1.0	4.6~2.7
	2.0	2.0	2.0	4.1~2.2

2.2 *Half-cell measurements*

Both the anode and cathode electrodes dismantled from the pristine batteries were re-assembled into button-cells with metallic Li as large-capacity counter electrode. These button-cells were characterized with the standard characterization procedures (see section 2.1) in order to determine the EMF curves of the individual electrodes. Note that the nominal capacity of the button cells is about 6 mAh. Therefore, the absolute value of the (dis)charging currents during characterization is much smaller than the currents used for complete batteries, while the C-rates were kept the same.

2.3 *X-ray Photoelectron Spectroscopy (XPS)*

In order to investigate the electrodes degradation mechanisms upon cycling, XPS measurements have been carried out on both the anodes and cathodes, dismantled from pristine and cycled batteries. The batteries were fully discharged at 0.5 C-rate before opening in an Argon glove box, and small pieces of the electrodes were cut and rinsed by pure solvent (Dimethyl Carbonate). The samples were transferred to the XPS equipment in a closed container in order to reduce the influence of moisture and air. XPS analyses were carried out with a Quantum 2000 ESCA spectrometer (Physical Electronics, USA), using Al K_α monochromatic irradiation (1486.6 eV) at a working pressure lower than $7 \cdot 10^{-8}$ bar. Depth profiling was carried out, using Ar ion-beam sputtering energy of 500 eV. The sputtering rate was equivalent to 0.26 nm/s on Ta_2O_5.

2.4 *Inductive Coupled Plasma-Optical Emission Spectrometry (ICP-OES)*

The ICP-OES method has been performed to determine the composition of the cathode. 0.5 g powder samples have been collected from the cathode dismantled from a pristine battery. 20 mL HCl (37.5%) and 1 mL H_2O_2 were added to the samples in order to dissolve the powders.

The etchants turn into light-blue solutions after 10 hours at 80ºC, leaving behind some undissolved suspensions (binders, conductivities, *etc.*). The suspensions were filtered and rinsed with deionized water for 3 times. The filtered solutions were collected and diluted to 1 L for the ICP measurements.

3. Results

3.1 ICP-OES results

The composition of the cathode was analyzed by ICP-OES measurements. Table 2 shows the ICP results of the cathode material. The measured concentrations of Ni, Mn and Co are 12.8, 7.83 and 5.38 µg/L, respectively, leading to a stoichiometric ratio of 5:3:2. Therefore, the chemical composition of the cathode material is concluded to be $LiNi_{0.5}Mn_{0.3}Co_{0.2}O_2$, also known as NMC(532).

Table 2. ICP measurement of the NMC cathode material.

Element	Ni	Mn	Co
Concentration (µg/L)	12.8	7.83	5.38
Ratio	5	3	2

3.2 EMF determination

Fig. 1 shows an example of the applied EMF determination. Fig. 1a illustrates the vertical extrapolation method. Blue symbols represent the voltages experimentally determined at various capacities (0.5, 0.75, 1.0 and 1.5 Ah) as a function of discharge current. As indicated by the lines, linear relationships are observed between the voltage and current at all discharge capacities, indicating that the equilibrium voltage (I = 0) can be obtained by linear extrapolation. The extrapolated voltages at I = 0 are indicated by the red symbols. Fig. 1b shows the horizontal extrapolation method. Blue symbols represent the capacities experimentally determined at various voltages (3.0, 3.1, 3.2 and 3.3 V) as a function of discharge current. Again, as indicated by the lines, linear relationships are observed between the capacity and the current, indicating that the maximum capacities (I = 0) at various discharge voltages can be obtained by linear extrapolation. The extrapolated capacities at I = 0 are indicated by the red symbols. Combining the extrapolation methods shown in Fig. 1a and b, the entire EMF curve as a function of SoC is then obtained (Fig. 1c). The maximum battery capacities at the cut-off voltage of 3.0 V at the

initial state (Q_{max}^0) and during cycling (Q_{max}^t) can easily be derived from the regular determined EMF curves [15-17, 27-29].
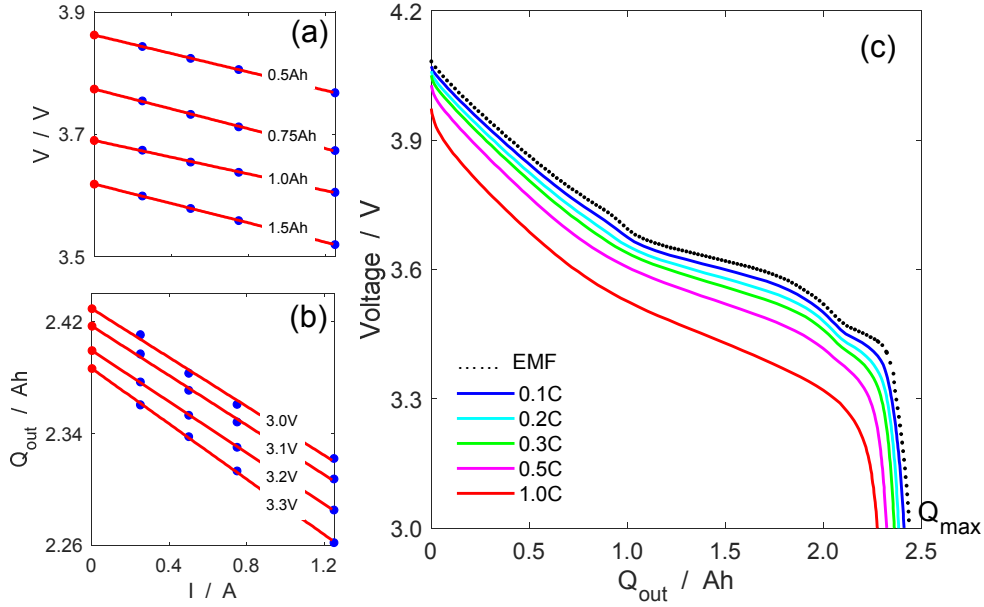
Fig. 1. (a) Battery voltage at various indicated discharge capacities as a function of discharge current (blue symbols) and corresponding voltages extrapolated to zero current (red symbols). (b) The battery capacities at various indicated discharge voltages as a function of discharge current (blue symbols) and the corresponding capacities extrapolated to zero current (red symbols). (c) Voltage discharge curves at various C-rates and extrapolated EMF curve (black dotted line).

3.3 Irreversible capacity losses ΔQ_{ir}

The irreversible capacity loss is calculated on the basis of the maximum battery capacities determined from the EMF curves, where $\Delta Q_{ir} = Q_{max}^0 - Q_{max}^t$. The charging current was fixed at 0.5 C for all cycling conditions. The influence of the charging current can therefore be ruled out in these experiments and the focus will be on the influence of the discharge current. Fig. 2a-c shows the development of ΔQ_{ir} for the NMC batteries at various discharge currents as a function of cycle number at different temperatures. Two regions, a logarithmic region (L-region) and an exponential region (E-region), can be discerned in Fig. 2a, corresponding to the aging temperature of 30ºC while only one region is observed at higher temperatures (Fig. 2b-c). The transition from the L-region to the E-region in Fig. 2a occurs at about 0.25 Ah, as indicated by the dashed line. In the L-region, the capacity loss increases logarithmically as a function of cycle number at all temperatures (Fig. 2a-c) and the degradation rates are significantly higher at 60ºC [16]. Interestingly, the development of ΔQ_{ir} at various discharging currents is almost

the same at 30℃ (Fig. 2a), indicating the independence of the capacity loss on the discharge conditions. However, the discharging-current dependence of ΔQ_{ir} becomes more distinct at 60℃ (Fig. 2c). From Fig. 2c it can be concluded that ΔQ_{ir} increases with decreasing current. The E-region is not so clear at 45℃ and is even completely absent at 60℃.
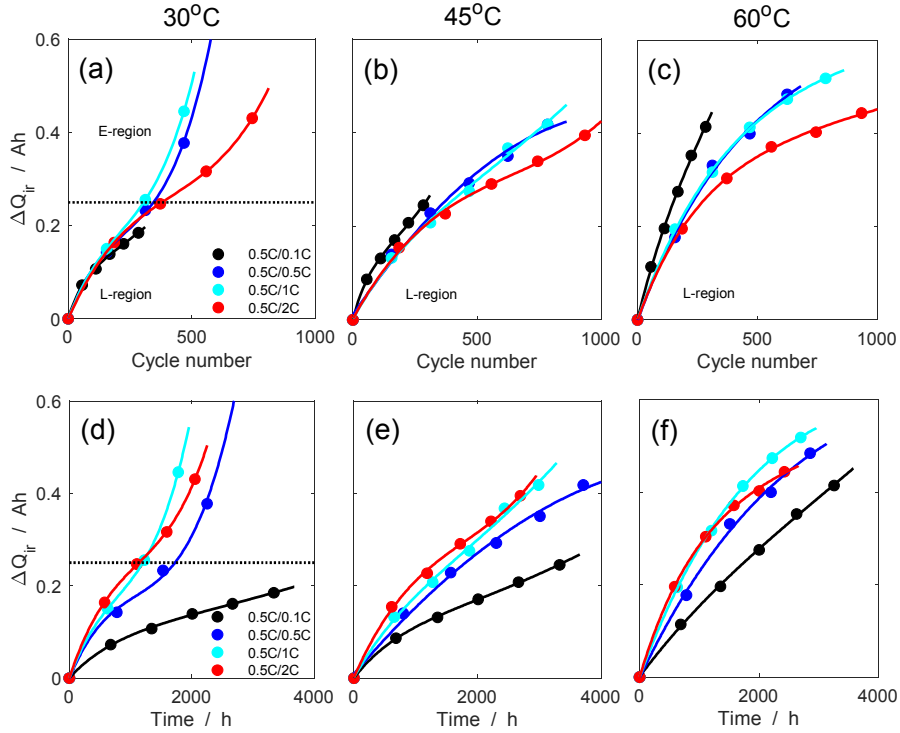
Fig. 2. Irreversible capacity loss ΔQ_{ir} as a function of cycle number (a-c) and time (d-f) at 30℃, 45℃ and 60℃. The charging current is 0.5 C while the discharging currents are 0.1, 0.5, 1.0 and 2.0 C-rate.

Fig. 2d-f shows the development of ΔQ_{ir} at various discharging currents and temperatures (30, 45 and 60℃) as a function of cycling time. Again, the E-region is very pronounced in Fig. 2d but becomes less clear in Fig. 2e and is even completely invisible in Fig. 2f. In contrast to the conclusions drawn from Fig. 2a-c, the current dependence of ΔQ_{ir} in the L-region is more pronounced at all temperatures (Fig. 2d-f), and clearly shows that ΔQ_{ir} increases with increasing current. The different conclusions obtained from Fig. 2a-c and Fig. 2d-f indicate that the cycle number and the time are two important parameters, both independently influencing the development of ΔQ_{ir} [16].

3.4 Half-cell analyses
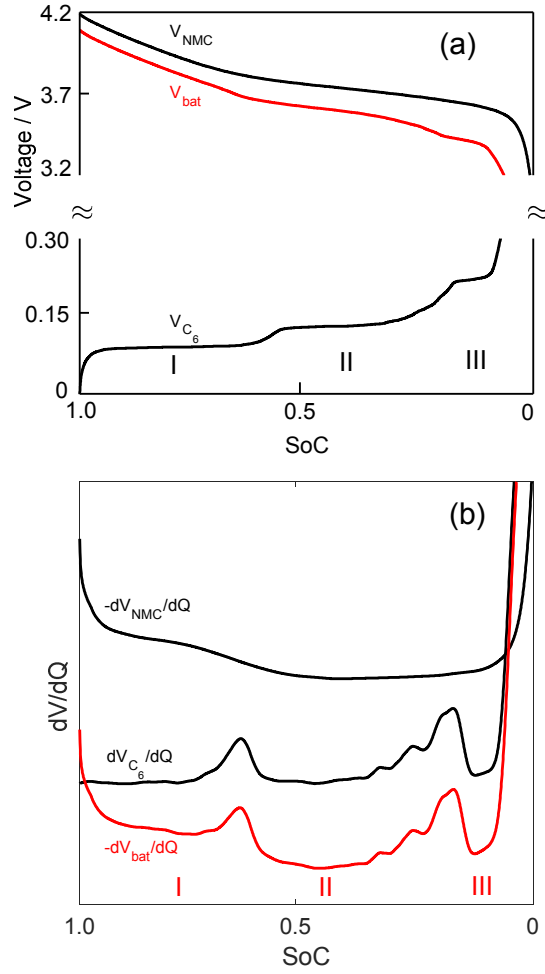
Fig. 3. (a) Cathode (V_{NMC}) and anode (V_{C_6}) voltage curves (black) of a dismantled pristine battery measured in half-cell experiments at 30ºC. The complete battery voltage curve V_{bat} (red) is calculated from $V_{bat} = V_{NMC} - V_{C_6}$. The voltage plateaus of the graphite electrode are indicated by I, II, and III. (b) Corresponding voltage derivative curves (dV_{bat}/dQ) calculated from V_{NMC}, V_{C_6} and V_{bat}. The depressions in the dV_{bat}/dQ curve (red) are corresponding to the plateaus in V_{C_6}.

Fig. 3a shows the individual electrode voltage curves at pristine conditions (black curves) and the resulting complete battery voltage curve (red curves) as a function of SoC. The individual electrode voltage curves (V_{NMC}, V_{C_6}) were measured with the corresponding electrodes *vs* metallic Li. Several voltage plateaus can be distinguished in the graphite voltage curve, which are attributed to the phase transition processes during delithiation. The complete battery voltage curve (V_{bat}) is calculated on the basis of V_{NMC} and V_{C_6}. Fig. 3b shows the corresponding voltage derivative curves calculated from V_{NMC}, V_{C_6} and V_{bat}. In order to facilitate a proper comparison, $-dV_{NMC}/dQ$, dV_{C_6}/dQ and $-dV_{bat}/dQ$ are plotted in Fig. 3b.

The $-dV_{NMC}/dQ$ curve is smooth, while several peaks and depressions are observed in the dV_{C_6}/dQ curve. The peaks are related to the sloping regions in the V_{C_6}-curve of Fig. 3a and the depressions correspond to the plateaus. Obviously $-dV_{bat}/dQ$ is a sum of $-dV_{NMC}/dQ$ and dV_{C_6}/dQ. The peaks and depressions observed in the $-dV_{bat}/dQ$ curve can therefore all be attributed to those found in the dV_{C_6}/dQ curve. The three regions indicated in the $-dV_{bat}/dQ$ curve are corresponding to the three plateaus in V_{C_6} (Fig. 3a).

3.5 dV_{EMF}/dQ analyses
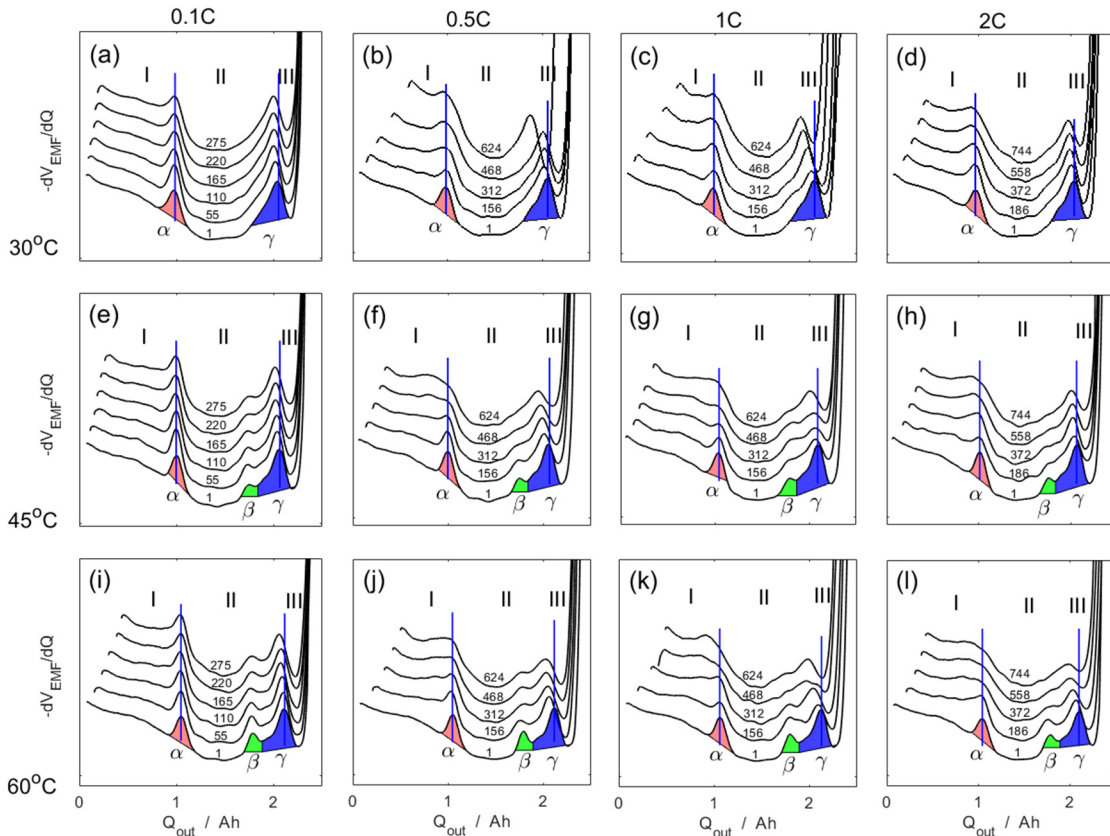
Fig. 4. The development of dV_{EMF}/dQ vs Q_{out} curves at various indicated temperatures and discharge currents as a function of the indicated cycle numbers. The vertical lines indicate the original position of the as-denoted α and γ peaks.

Fig. 4 shows the dV_{EMF}/dQ curves which are obtained from the regularly determined EMF curves at 30°C (Fig. 4a-d), 45°C (Fig. 4e-h) and 60°C (Fig. 4i-l) at various cycling currents and as function of the indicated cycle numbers. The three indicated depressions I, II and III are related to the plateaus of the graphite electrode and the peaks in the dV_{EMF}/dQ curves are attributed to the sloping regions in the EMF curves, as discussed above in relation to Fig. 3.

The peaks in the dV_{EMF}/dQ curves are denoted as α (red), β (green) and γ (blue). Interestingly, the β peak is hardly observed in Fig. 4a-d, but becomes visible in Fig. 4e-h and are even more distinct in Fig. 4i-l. This may be due to the thermal instability of LiC_{18} and LiC_{24} at lower temperatures. The α peak becomes less visible upon cycling, especially at higher C-rates and elevated temperatures. Since the β peak is invisible at 30ºC, region II is here defined between the α and γ peaks.

All curves in Fig. 4 are aligned with respect to the α peak at approximately 1.0 Ah in order to facilitate a proper analysis of the width of regions I and II. The two vertical lines in each figure represent the initial positions of regions I and II. A decline in the lengths of region I (ΔQ_I) and region II (ΔQ_{II}) is observed under all aging conditions. It can be seen that ΔQ_I is small at 30ºC (Fig. 4a) but becomes significant at 60ºC (Fig. 4i), indicating a strong temperature dependence. In contrast to the behavior of ΔQ_I, the temperature influence on ΔQ_{II} is negligible for the present aging conditions.
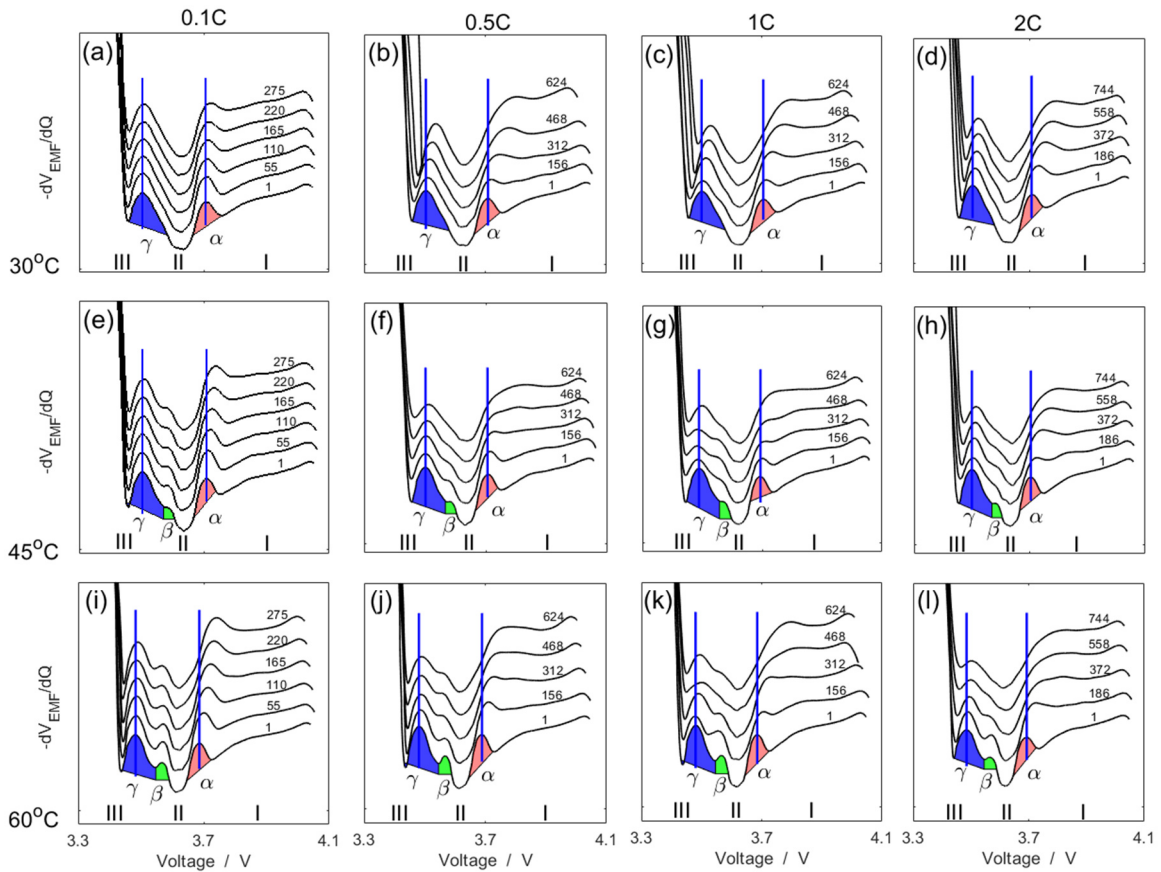
Fig. 5. Development of dV_{EMF}/dQ vs voltage curves at the various indicated temperatures and cycling currents. Vertical lines indicate the original positions of the α and γ peaks.

In order to get more direct voltage information, the voltage derivative curves discussed in Fig. 4 are replotted in Fig. 5 as a function of voltage. Similar to Fig. 4, the original position of both α and γ peaks are indicated by vertical lines. It can be seen that the γ peak remains almost at the same position upon ageing at 30°C and 0.1C (Fig. 5a). However, it shifts to higher voltages when the discharge current is increasing due to the increased battery polarization (Fig. 5b-d). The influence of the discharging current on the position of the γ peak is almost negligible at 45 (Fig. 5e-h) and 60°C (Fig. 5i-l). On the other hand, the position of the α peak is more clearly dependent on the temperature and current. Although the α peak also remains at the same position upon aging at 30°C with 0.1C (Fig. 5a), it starts to shift significantly towards higher voltages at higher temperature and discharge current. Moreover, the shape of the α peak is dramatically deformed upon ageing to become very wide at higher currents, making it difficult to distinguish.

3.6 XPS analyses

3.6.1. Anode analyses

The evolution of the C1s spectra of a pristine graphite electrode as a function of the indicated sputtering time (interval between the curves is 30 s) is shown in Fig. 6a and that of a cycled graphite electrode at 30°C in Fig. 6b. For clarity reasons, only the C1s spectra at t = 30 s (red) are deconvoluted with respect to the peaks of C_6 and the various SEI components. The C1s peak of C_6 is located at 284.5 eV, the reflections located at higher binding energies are assigned to various components of the SEI layers [30]. In the pristine state (Fig. 6a) the signal of SEI components are only minor. The peak at 285.5 eV is corresponding to $\underline{C}-H$, that at 286.4 eV is attributed to $\underline{C}-O-\underline{C}$, the peak at 287.6 eV can be assigned to $\underline{C}=O$ and that at 289.3 eV is attributed to COOR. The last peak at 291.4 eV is related to CO_3^{2-} ions. It is worthwhile to note that the $\pi - \pi^*$ shave-up satellite of C1s (weak peak) is also located at approximately 291 eV [31]. The peak at 291.4 eV is therefore a composite signal of both CO_3^{2-} ions and the $\pi - \pi^*$ shave-up satellite. After ageing (Fig. 6b) the C1s signals of various SEI components become more pronounced. In contrast, the graphite signal in Fig. 6b becomes much weaker than in Fig. 6a, indicating that the graphite electrode is suffering from a significant growth of the SEI layers upon aging. At higher sputtering times the intensity of the graphite C1s spectra becomes more and more significant, while the signal of the SEI components becomes weaker as the bare graphite surface has been reached. Comparing Fig. 6a and b it can clearly be seen that the thickness of the SEI layers has increased upon aging.
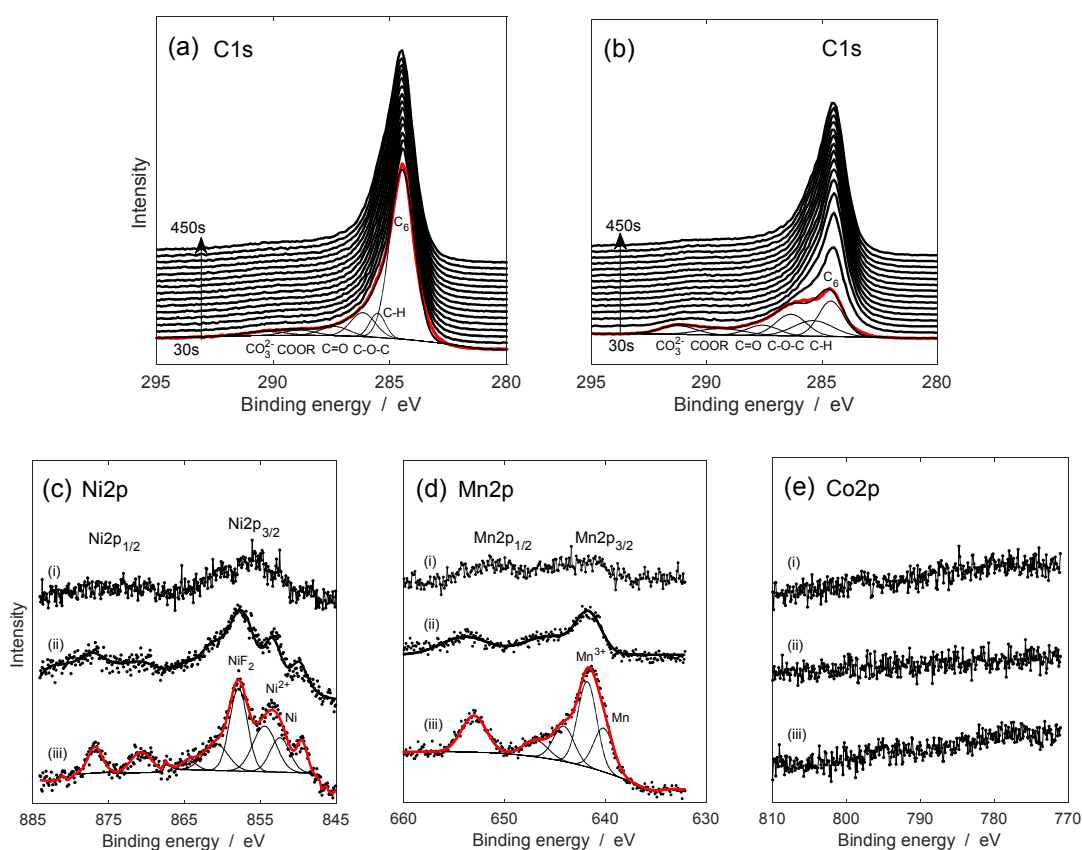
Fig. 6. Development of the C1s spectra of a dismantled graphite electrode in the pristine state (a) and after cycling at cycle 275 and 0.1C, 30°C (b) as a function of sputtering time. The Ni2p (c), Mn2p (d) and Co2p (e) spectra of dismantled graphite electrodes. (i) spectra at the surface of pristine graphite; (ii) at the surface of aged (n = 275, 0.1C, 30°C) graphite, and (iii) after sputtering (30 s) aged graphite.

Fig. 6c-e shows the development of the Ni2p (c), Mn2p (d) and Co2p (e) spectra of dismantled graphite electrodes. Curves (*i*) in Fig. 6c-e shows the respective Ni, Mn and Co spectra of a pristine graphite electrode at the surface. Curves (*ii*) represent the surface of an aged graphite electrode at 30°C, 0.1C, and curves (*iii*) show the spectra of the aged electrode after sputtering for 30 s. Hardly any information can be obtained from curves (*i*) in Fig. 6c-e. It can therefore be concluded that no Ni, Mn and Co elements are present at the pristine graphite surface. However, the signals of Ni and Mn are clearly observed at the cycled graphite surface (curves (*ii*) in Fig. 6c and d, respectively). The intensity of the Ni (c) and Mn (d) signals is even more pronounced after sputtering (curves (*iii*)). Interestingly, no Co2p signal can be observed in Fig. 6e, neither for the pristine graphite (curves (*i*)) nor for the aged graphite electrode (curves (*ii*) and (*iii*)).

For clarity reason, only the deconvoluted curves (*iii*) are shown in Fig. 6c-d. Two clear Ni $2p_{3/2}$ peaks can be distinguished in Fig. 6c. The first Ni $2p_{3/2}$ core level peak at 853.5 eV compares well to the theoretical value of 852.8 eV for metallic Ni [32], and 854.5 eV for Ni^{2+} ions [33], indicating the co-existence of the both components. Another sharp peak at 858 eV in curve (*iii*) of Fig. 6c can be assigned to NiF_2 [34]. The two weak shake-up satellite peaks located in 861.5 and 864.5 eV can be considered as a fingerprint for Ni^{2+} and NiF_2, respectively. The two major peaks at 641.4 eV and 653.1 eV observed in curve (*iii*) of Fig. 6d can be attributed to Mn $2p_{3/2}$ and Mn $2p_{1/2}$, respectively. The Mn $2p_{3/2}$ core peak is fitted with two sub-peaks. The peaks at 640 and at 641.8 eV are attributed to metallic Mn and Mn^{3+} (or Mn^{2+}), respectively. Two weak satellite peaks are observed at 644.1 and 648 eV, which confirm the co-existence of metallic Mn and Mn-cations, respectively. In order to have a clear overview, the binding energies of the various elements summarized from literature and those obtained from the above described measurements are listed in Table 3.

Table 3. Binding energies of various elements from literature and measurements.

	$P_{3/2}$ /eV	References	$P_{1/2}$ /eV	References
Ni^0	852.4 ~ 852.7	[32, 33, 35, 36]	870	*
Ni^{2+}	854 ~ 855	[37-47]	871.9 ~ 872.4	[40-43]
Ni^{3+}	855.3 ~ 856.5	[48, 49]	874	[43, 44]
NiF_2	857.2 ~ 857.9	[36, 46, 50]	877	*
Co^{3+}	779.5 ~ 780.5	[37, 41, 47, 51, 52]	794.8 ~ 795.4	[51-53]
Co^{4+}	782.1	[43]	796.6	[43]
Mn^0	640.3	*	652.9	*
Mn^{2+}	641.4	*	653.1	*
Mn^{4+}	642 ~ 642.8	[38, 39, 41, 42, 46, 47]	653.7 ~ 654.5	[42, 43]

Note: * value measured in this work.

3.6.2. Cathode analyses
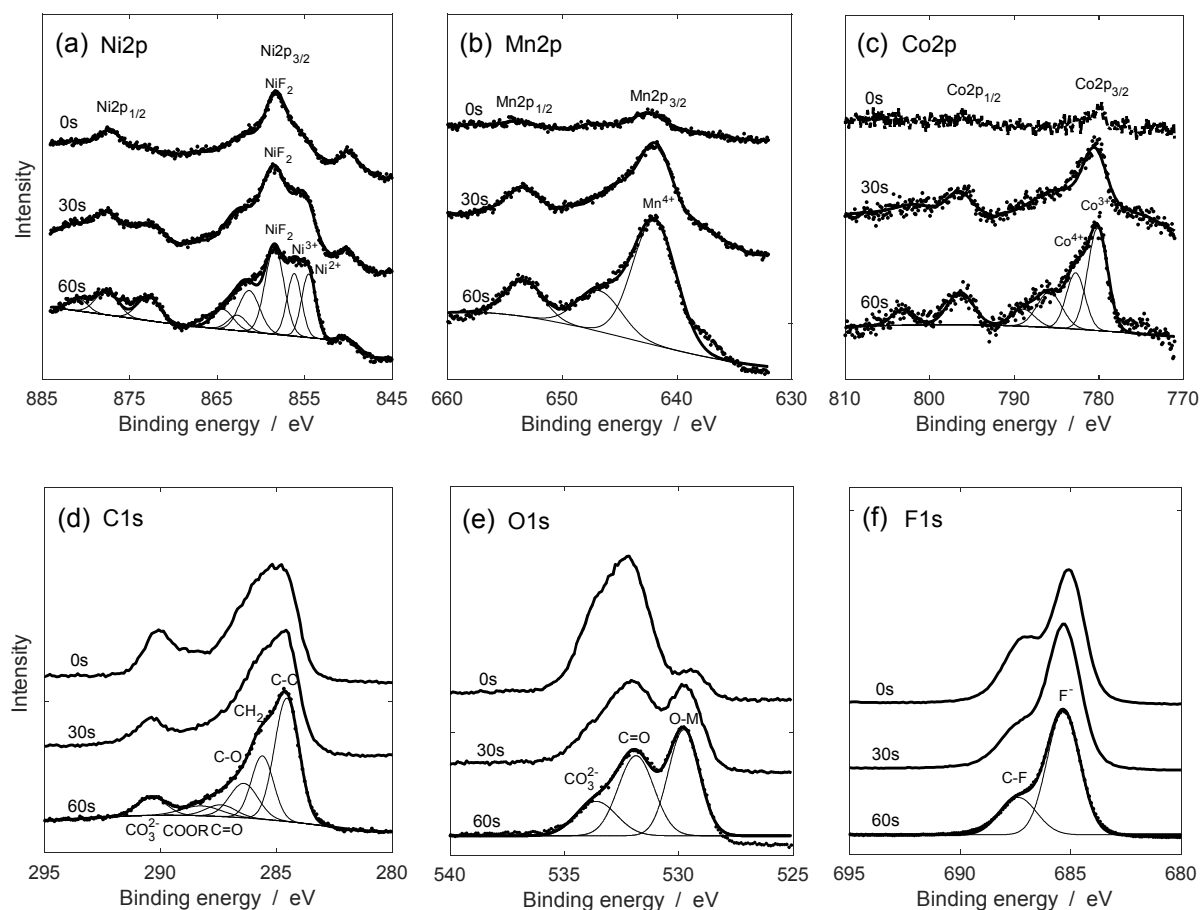
Fig. 7. The Ni2p (a), Mn2p (b), Co2p (c), C1s (d), O1s (e) and F1s (f) spectra of an aged cathode (n = 275 0.1C, 30°C) at various indicated sputtering times.

In order to get more depth information, XPS analyses have also been carried out on an aged cathode as a function of sputtering time. Fig. 7 shows the Ni2p (a), Mn2p (b), Co2p (c), C1s (d), O1s (e) and F1s (f) spectra of the cathode after ageing with a charging current of 0.5C and discharging current of 0.1C at 30°C. Different curves are corresponding to the various indicated sputtering times. As shown in Fig. 7a, the Ni 2p spectrum reveals two main peaks at 858 and 877.5 eV when no sputtering has been carried out (0 s), which are attributed to the $Ni2p_{3/2}$ and $Ni2p_{1/2}$ core levels of NiF_2, respectively [54]. The $Ni2p_{3/2}$ main peaks of Ni^{2+} and Ni^{3+} at 854.7 and 856.3 eV, respectively, are hardly detected at the surface of the cathode. However, the intensity of these two peaks significantly increases after sputtering. The broad shoulder at about 862 eV has been further deconvoluted with three sub-peaks at 861.5, 862.7 and 864.5 eV. These three peaks are corresponding to the satellites of Ni^{2+}, Ni^{3+} and NiF_2, respectively. The main peaks and the satellites are assigned to so-called "shakeup" effect [37, 40].

Fig. 7b shows the development of the Mn2p spectra of the cathode. The signal of Mn2p is hardly observed at the cathode surface at t = 0 s. However, it becomes clearly visible after

sputtering for 30 s and becomes very pronounced after 60 s sputtering. The binding energies at 642.2 and 653.2 eV are attributed to the Mn $2p_{3/2}$ and Mn $2p_{1/2}$ core levels of Mn^{4+} in the lattice structure, respectively. The weak shoulder peak observed at 647.2 eV is corresponding to the satellite peak of Mn^{4+}.

Fig. 7c shows that the development of the Co2p spectra is very similar to that of the Mn2p spectra. Almost no signal can be detected at the cathode surface, but the signals become much stronger after sputtering. The peaks at 780 and 796.4 eV are corresponding to Co $2p_{3/2}$ and Co $2p_{1/2}$ core levels of Co^{3+} in the lattice structure, respectively. The Co $2p_{3/2}$ core levels of Co^{4+} at 782.7 eV has also been identified, indicating the co-existence of Co^{3+} and Co^{4+} in the lattice structure. The satellite peaks for Co^{3+} and Co^{4+} at 786 and 789 eV are attributed to the shakeup effect which is strongly dependent on the oxidation state and the environment of the metal [52].

From Fig. 7a-c it can be concluded that a Cathode-Electrolyte-Interface (CEI) layer is clearly formed at the cathode surface upon aging. NiF_2 is one of the various components constituting this layer. In order to have an in-depth understanding of the composition of the CEI layer, the C1s, O1s and F1s spectra have also been analyzed in more detail.

Fig. 7d shows the development of the C1s spectra of the aged cathode at various sputtering times. For clarify, only the deconvoluted spectrum is shown at t = 60 s. The peak at 284.5 eV is attributed to the $\underline{C}-C$ group in the carbon black and that at 285.6 eV to the $\underline{C}–H$ group in the organic compounds. The peak at 286.5 eV is attributed to $\underline{C}–O$ group, that at 287.5 eV to $\underline{C}=O$ and that at 289.6 eV is related to the $\underline{C}OOR$ group in the organic compounds. The final peak at 290.5 eV is considered to be a composite signal of the $\underline{C}O_3^{2-}$ anion and $\pi - \pi^*$ shave-up satellite. The intensities of various components (*e.g.*, $\underline{C}=O$, $\underline{C}O_3^{2-}$ and $\underline{C}$-H) decrease upon sputtering since the surface of the cathode materials is reached. However, the intensities of all components are still considerably high after sputtering 60 s due to the porous nature of the cathode.

Fig. 7e shows the development of the O1s spectra of the aged cathode. Three different binding energies, corresponding to the lattice O (529.7 eV, the $\underline{O}–M$ in the cathode material), $C=\underline{O}$ (531.8 eV) and $\underline{O}–C=O$ (533.8 eV) can clearly be identified. The peak intensity of $\underline{O}–M$ is negligible compared to that of $C=\underline{O}$ and $\underline{O}–C=O$. However, the peak intensity of $\underline{O}–M$ significantly increases after sputtering while the intensities of $C=\underline{O}$ and $\underline{O}–C=O$ dramatically decreases. This is because the various components at the cathode surface are removed after sputtering and the bare cathode active materials are reached. Combining the results of Fig. 7d and e, it can be concluded that the carbonate-related Li salts are part of the CEI layer.

Fig. 7f shows the development of the F1s spectra of the aged cathode. Two different F atoms can be identified in the spectra. The peak at 685.3 eV is attributed to F^- and that at 687.5 eV to

C−E. The relative intensity of the C−E peak decreases with respect to that of F⁻ upon sputtering. C−E is attributed to the binder (PVdF) and the F⁻ anion is considered to originate from NiF_2 and/or LiF compounds. The decline of the C−E peak intensity can be explained by the decrease of the binder after sputtering. However, the amount of F⁻ anion seems to be constant after sputtering since the intensity of F⁻ remains almost constant upon sputtering. This striking result indicates that the distribution of F⁻ anions, such as NiF_2, is evenly distributed in the CEI layer.

4. Discussion

4.1 Irreversible capacity loss ΔQ_{ir}

Degradation of Li-ion batteries are related to many ageing processes, such as SEI formation at the anode, losing the mechanical integrity of the electrodes, electrolyte decomposition, *etc*. The degradation mechanisms can often be attributed to the loss of cyclable lithium and are strongly dependent on the battery chemistries. For example in C_6/LiFePO$_4$ (LFP) batteries, the SEI formation is considered to be the main reason for the capacity loss [55]. On the other hand, in C_6/LiNi$_x$Co$_y$Mn$_z$O$_2$ (NMC) batteries the capacity loss does not originate from a single ageing process but rather combines various processes and their interactions. Apart from the intrinsic chemical properties of the battery system, the ageing conditions also have a significant influence on battery degradation. In general, elevated temperatures, larger cycling currents and higher states-of-charge will accelerate battery ageing. However, the results shown in Fig. 2 deviate from the general sense of ΔQ_{ir} development. Only one region (L-region) can be discerned at elevated temperatures at 60ºC (Fig. 2c) while two regions can clearly be distinguished at lower temperatures (Fig. 2a and d). These two regions at 30ºC indicate that there are at least two different temperature-related mechanisms, determining battery degradation, which are denoted as Mechanism I and II. Mechanism I is responsible for the capacity loss over a wide temperature range while Mechanism II accelerates degradation of the cells only at lower temperatures. Mechanism II is related to kinetic degradation, including resistance increase [54], overpotential development, *etc*. The effect of mechanism II on the capacity loss is significant at lower temperatures due to kinetic retardation and polarization increases.

In L-region, the total irreversible capacity loss ΔQ_{ir} can be related to calendar ageing (ΔQ_{ir}^{ca}) and cycling-induced ageing (ΔQ_{ir}^{cr}) [16]. ΔQ_{ir}^{ca} is only ageing-time dependent while ΔQ_{ir}^{cr} depends on the cycle number [16]. In the present work, the charging current is always kept the same while only the discharge current varies. The difference of the total ageing time is therefore

only determined by the discharging currents. At a given cycle number, the total ageing time increases with decreasing discharge current. ΔQ_{ir}^{cr} remains the same at the various discharging currents since ΔQ_{ir}^{cr} only depends on the cycle number. However, ΔQ_{ir}^{ca} will increase with decreasing discharging currents. Therefore, the deviation of ΔQ_{ir} at the various discharging currents must be attributed to ΔQ_{ir}^{ca}, which is only a function of ageing time. At 30ºC (Fig. 2a), ΔQ_{ir} is almost constant for the various discharging currents at a given cycle number. It is indicated that the calendar ageing during discharging is negligible at 30ºC. The total irreversible capacity loss is therefore almost current independent. However, when temperature increases to 45ºC (Fig. 2b), ΔQ_{ir} starts to deviate from each other at the various discharge currents. This indicates that calendar ageing during discharging becomes more considerable at 45ºC. The deviation of ΔQ_{ir} at various discharging currents becomes more clear at 60ºC, as shown in Fig. 2c, indicating that calendar ageing during discharging is more significant at 60ºC. Many ageing processes such as SEI formation, cathode dissolution *etc*., can contribute to the calendar ageing. These processes can be accelerated by elevated temperatures, following Arrhenius law.

At a given cycle time, the cycle number increases with increasing discharge current. ΔQ_{ir}^{ca} remains constant at various currents since ΔQ_{ir}^{ca} only depends on the cycle time. However, ΔQ_{ir}^{cr} will increase at higher discharge currents since the cycle number increases. Therefore, the deviation of ΔQ_{ir} at the various discharging currents can only be attributed to ΔQ_{ir}^{cr}. As can be seen from Fig. 2d-f, ΔQ_{ir} dramatically increases at elevated temperatures, indicating that ΔQ_{ir}^{ca} becomes more dominant at elevated temperatures.

4.2 EMF derivative (dV_{EMF}/dQ) analysis

The electrode potential is a function of the Li stoichiometry (State-of-Charge (SoC)) in the electrode materials, and is determined by the material structure evolution upon (dis)charging. The electrode potential development can therefore reveal useful information about the structure evolution of the electrode materials. Voltage derivative analysis provides an efficient way to zoom in into the electrode potential development. The voltage discharge curves and dV/dQ curves of the individual electrode as well as the full battery have been shown in Fig. 3. The peaks in the dV/dQ curves (Fig. 3b) are corresponding to the slopes on the voltage curves (Fig. 3a) while the depressions are related to the plateaus. Due to the series configuration of the individual electrodes in a full cell, the amount of the charge transferred through both electrodes upon (dis)charging is always the same, and is given by the total current flowing through the complete cell. The voltage derivative curve of the full battery can therefore be written as

$$\frac{dV_{bat}}{dQ} = \frac{d(V_{NMC} - V_{C_6})}{dQ}$$

$$= \frac{dV_{NMC}}{dQ} - \frac{dV_{C_6}}{dQ}. \qquad (1)$$

Since plateau II observed in the dV_{bat}/dQ curves always originates from the second plateau in the dV_{C_6}/dQ curve, the decrease of plateau II denoted as $\Delta Q_{Li,II}$ in the dV_{bat}/dQ curve is therefore considered to be an indicator of graphite degradation. The graphite electrode degradation can be quantified by [15]

$$\Delta Q_{C_6} = \frac{\Delta Q_{Li,II}}{x_{II}}, \qquad (2)$$

where x_{II} represents the capacity ratio of the plateau II with respect to the whole graphite electrode capacity. $\Delta Q_{Li,II}$ can be obtained from the dV_{EMF}/dQ *vs* Q curves (Fig. 4). From Fig. 4 it can be concluded that the influence of temperature on graphite degradation is not obvious, however, the influence of the current is very clear.

To distinguish cathode degradation in the dV_{bat}/dQ curves remains challenging since no pronounced characteristics can be observed from the dV_{NMC}/dQ curves. However, changes in the cathode electrode potential will influence the shape and location of the peaks observed in the dV_{bat}/dQ *vs* V curves (Fig. 5), which also provides more insight into the cathode degradation. The advantage of dV_{EMF}/dQ *vs* V curves is that it can directly provide information of the voltage development. The peaks in dV_{EMF}/dQ *vs* V curves can again be attributed to the slopes in the voltage curves and the depressions to the plateaus in the voltage curves. The evolutions of the peaks and the plateaus are consequences of the development of the electrode balancing. Comparing Fig. 5a, e and i, it can be seen that the γ peak keeps almost at the same position while the α peak shifts to higher voltages. This makes the voltage gap of plateau II wider. The increase of this voltage gap can be related to:

(i) The cycling range of the cathode shifts to more positive voltages due to Li immobilization at the surface of the graphite electrode;

(ii) The cathode voltage curve shrinks and shifts to lower battery SoC due to cathode degradation.

Comparing Fig. 5a-d it can be seen that the width of plateau II increases as a function of current, indicating the above two processes become more severe at higher currents. Interestingly,

both the γ and α peaks shift towards higher voltages when the current is higher than 0.5C-rate. The shift of γ and α peaks are caused by:

(i)   The cycling range of the cathode shifts to the more positive voltages due to Li immobilization at the surface of the graphite electrode;

(ii)   The anode voltage curve shrinks and shifts to higher battery SoC due to anode degradation;

(iii)   The cathode voltage curve shrinks and shifts to lower battery SoC due to cathode degradation.

The degradation mechanisms of the individual electrodes are still under discussion. It is generally accepted that the SEI formation at the graphite electrode is mainly responsible for the Li immobilization. Strain generated during the (de)lithiation processes was considered to be the main origin for the graphite structure decay. Additionally, Li and co-workers [17] observed considerable graphite degradation even under non-cycling, storage, conditions when the rocking-chair process of lithium is excluded. Transition metal dissolution and subsequent precipitation at the anode was also considered to be important, influencing the SEI formation and hence graphite degradation at elevated temperatures [17]. The cathode degradation mechanism is still disputable. Cathode dissolution process is believed to be driven by residual protons on ppm level in the electrolyte. Apart from metal dissolution, irreversible phase transition during cycling is considered to be another degradation mechanism of cathode materials. NMC material experiences a phase transition from the rhombohedral space group $R\bar{3}m$ (initial "O3" phase) to the monoclinic space group C2/m ("O1" phase) when the charge voltage becomes beyond 4.4 V *vs* Li^+/Li [23].

So-called half-cell measurements are often used to quantify electrode(s) degradation. However, this method is generally found to be inaccurate due to the poor reproducibility of the half-cell characteristics. Making use of reference electrodes is another method to investigate degradation of the individual battery electrodes. Nevertheless, the stability of the reference electrode often remains challenging. Moreover, batteries have to be opened in both methods, leading to inconvenience and cell damage. A non-destructive method to identify the individual electrode degradation is therefore highly welcome. The method presented in Figs. 4 and 5 provides a possibility to accurately unravel the individual electrodes degradations *in situ*, without damaging the battery.

4.3 SEI formation at the C₆ electrode

The SEI formation at the graphite electrode induced by ageing is confirmed by the XPS analyses shown in Fig. 6a-b. The SEI layer is composed of products reduced from the various solvents present in the electrolyte. Ethylene carbonate (EC), propylene carbonate (PC), dimethyl carbonate (DMC) and diethyl carbonate (DEC) are the most popular solvents in commercial electrolytes. Typical reduction reactions of these solvents can be represented by the following reactions [30]: Reduction of EC takes place, according to

$$EC + 2Li^+ + 2e^- \longrightarrow CH_2=CH_2 \text{ (g)} + Li_2CO_3 \text{ (s)},$$

and/or

$$2EC + 2Li^+ + 2e^- \longrightarrow CH_2=CH_2 \text{ (g)} + CH_2(OCO_2Li)CH_2OCO_2Li \text{ (s)}; \tag{3}$$

Reduction of DMC occurs, according to

$$CH_3OCO_2CH_3 + Li^+ + e^- \longrightarrow CH_3OLi \text{ (s)} + CH_3OCO^\cdot,$$

or

$$CH_3OCO_2CH_3 + Li^+ + e^- \longrightarrow CH_3OCO_2Li \text{ (s)} + CH_3^\cdot. \tag{4}$$
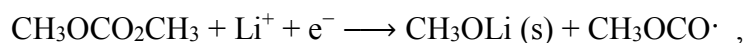
The $CH_3OCO^\cdot$ and $CH_3^\cdot$ radicals can be freely re-assemble, forming C_2H_6 or $(CH_3OCO)_2$ or CH_3OCOCH_3. Reduction of DEC can be represented by

$$CH_3CH_2OCO_2CH_2CH_3 + Li^+ + e^- \longrightarrow CH_3CH_2OLi \text{ (s)} + CH_3CH_2OCO^\cdot$$

or

$$CH_3CH_2OCO_2CH_2CH_3 + Li^+ + e^- \longrightarrow CH_3CH_2OCO_2Li \text{ (s)} + CH_3CH_2^\cdot \tag{5}$$

The $CH_3CH_2OCO^\cdot$ and $CH_3CH_2^\cdot$ radicals can re-assemble into C_4H_{10} or $(CH_3CH_2OCO)_2$ or $C_2H_5OCOC_2H_5$, respectively. Reduction of PC can be represented by

$$PC + 2Li^+ + 2e^- \longrightarrow CH_3CH_2=CH_2 \text{ (g)} + Li_2CO_3 \text{ (s)}$$

and/or

$$2PC + 2Li^+ + 2e^- \longrightarrow CH_3CH_2{=}CH_2 \text{ (g)} + CH_3CH(OCO_2Li)CH_2OCO_2Li \text{ (s)} \qquad (6)$$
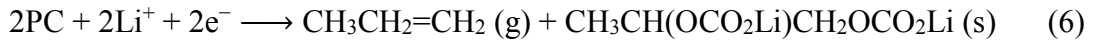
The various components identified in the XPS spectra in Fig. 6a-b are in line with the electrolyte degradation mechanisms proposed in Eqs. 3-6. The growth of the SEI layer is confirmed by the depth profiles of the C1s spectra shown in Fig. 6b. It should be noted that after dismantling and rinsing the electrodes, some of the SEI layers can be dissolved or detached. Therefore the real thickness of the SEI layers might deviate from what has been detected by XPS.

Apart from solvent reduction, cathode dissolution and subsequent precipitation at the anode can also contribute to the SEI formation. The transition metal ions dissolved from the cathode can pass through the electrolyte and arrive at the anode, forming different products according to

$$Me^{2+} + 2e^- \longrightarrow Me \qquad (7)$$

and

$$Me^{2+} + 2F^- \longrightarrow MeF_2. \qquad (8)$$
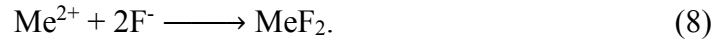
Me represents the transition metal ions (Me = Ni or/and Mn). As discussed in Fig. 6c, both metallic Ni and NiF_2 are confirmed by XPS analyses. The deposited Ni particles may block the graphene layers which leads to the inaccessibility of the graphite electrode and finally leads to graphite degradations.

Both the solvent reduction and metal precipitation under various ageing conditions have been simulated by Li *et al.* [55-57]. From the proposed ageing model it has been concluded that the SEI formation is temperature-dependent. An Arrhenius relationship has been adopted to describe the relationship between the temperature and the SEI formation processes [55].

4.4 CEI formation at the NMC electrode

Transition metal dissolution is a very common process in NMC systems. Metal dissolution in various cathode materials at 55°C has been reported by Choi and Manthiram [58]. Li *et al.* confirmed cathode dissolution under battery operating conditions by XPS analyses [54]. Apart

from metal dissolution, the formation of a so-called Cathode-Electrolyte-Interface (CEI) at the cathode surface is considered to be another well-accepted degradation mechanism. The composition of the CEI includes (in)organic Li salts (LiF, LiCOOR), metal fluoride compounds (*i.e.* NiF_2), *etc*. The Li salts are believed to be formed from electrolyte oxidation and $LiPF_6$ decomposition. The formation of metal fluoride compounds is initiated by the transition metal dissolution process, which is driven by residual HF present in the electrolyte. Two possible mechanisms have been proposed to explain the reaction between HF and cathode materials [54]. The first mechanism can be represented by

$$MeO + 2HF \longrightarrow MeF_2 + H_2O, \tag{9}$$

where Me denotes the transition metals (Ni, Co, Mn) and MeO the metal-oxygen slabs in the cathode material. In the NMC(532) system, NiO can react with HF, leading to NiF_2 observed in the XPS spectra of Fig. 7. The second possible mechanism can be described by

$$4HF + Li_2O\text{-}MeO \longrightarrow Me^{2+} + 2H_2O + 2LiF + 2F^-. \tag{10}$$

According to the above mechanism, the transition metal ions are dissolved into the electrolyte and finally transported to the anode. Interestingly, H_2O is always formed in the both mechanisms. H_2O can accelerate the $LiPF_6$ decomposition and induces the formation of HF, according to

$$LiPF_6 + H_2O \longrightarrow LiF + 2HF + POF_3. \tag{11}$$
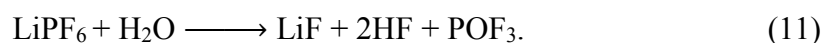
Combining Eqs. 9-11, it can be concluded that residual H_2O in the electrolyte plays a role as catalyst in the cathode dissolution processes.

The other CEI components has been analyzed by XPS. The analyses in Fig. 7d-f confirm the existence of the $\underline{C}$-C group (284.5 eV), $\underline{C}$-H (285.6 eV), $\underline{C}$-O (286.5 eV), $\underline{C}$=O (287.5 eV), $\underline{C}$OOR (289.6 eV) and $\underline{C}O_3^{2-}$ (290.5 eV). The C-C group is attributed to carbon black, which was added in the electrode slurry to improve the electronic conductivity of the electrode materials. The C-H, C-O, C=O and COOR groups are attributed to the organic compounds oxidized from the electrolyte solvents or other reductive species in the electrolyte [54]. The origins of CO_3^{2-} at cathode is still under discussion. A well acceptable explanation is that CO_3^{2-} is formed by the transformation of CO_2 which is oxidized from CO [59].

4.5 Ageing model

From the above discussion it can be concluded that many degradation processes are involved in battery ageing. The discussed ageing mechanisms of $C_6/LiMn_xNi_yCo_zO_2$ batteries are summarized in Fig. 8. At the anode, the Solid-Electrolyte-Interface (SEI) formation is considered to be the most important degradation process. The SEI layer is formed by the products from electrolyte reduction at the anode. It is widely accepted that the SEI layer is composed of two sublayers: a dense inner layer and a porous outer layer [56]. The inner-SEI layer cannot allow solvent to penetrate, preventing exfoliation of the graphite structures by solvent co-intercalation. The inner-SEI layer is mainly composed of inorganic Li salts while the outer-SEI layer is composed of organic Li salts. Some SEI cracks will be formed during charging due to the graphite electrode expansion. The new SEI formation at these cracks will lead to irreversible capacity loss ΔQ_{ir}^{cr} while the continuous SEI formation on the constant covered SEI surface will lead to ΔQ_{ir}^{ca}.
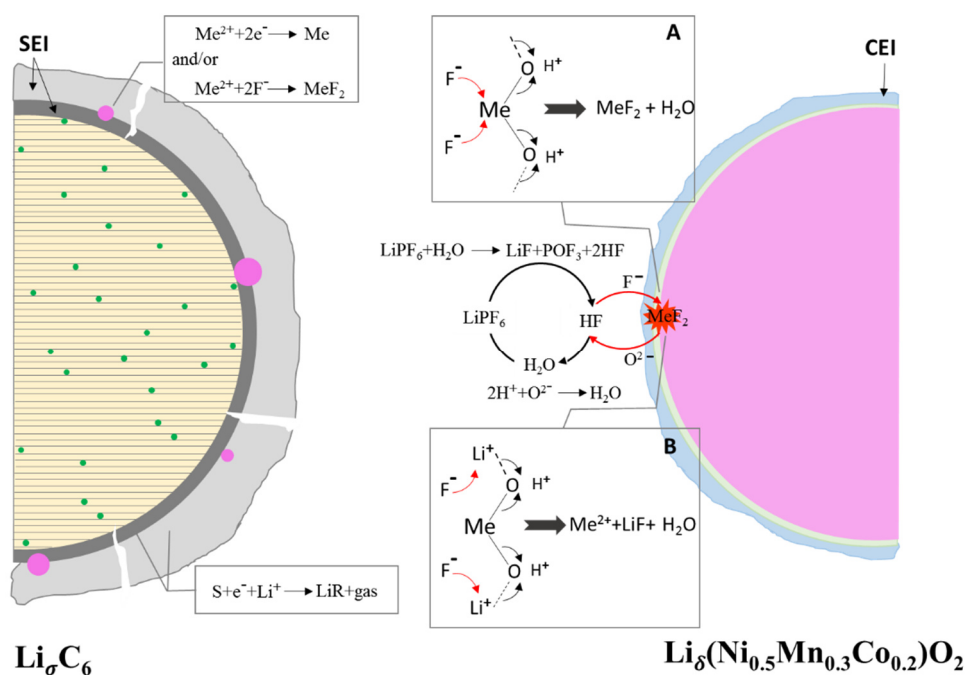
Fig. 8. Schematic representation of the various ageing mechanisms of $C_6/LiMn_{0.5}Ni_{0.3}Co_{0.2}O_2$ Li-ion batteries.

Apart from the various Li salts, metallic transition metal particles as well as transition metal compounds are also important components of the SEI layers. The transition metal ions dissolved from the cathode can pass through the electrolyte and be reduced at the anode surface. These

metal particles can block the graphite layered structure and will lead to enhanced graphite degradations. Li *et al*. [55] has simulated the formation of the SEI layer under various ageing conditions in the C_6/LiFePO$_4$ battery system. It has been concluded that the thickness of the inner-SEI layer generally determines the growth of the total SEI layer. In addition, crack formation and precipitation of metallic particles inside the SEI layer can accelerate the SEI formation and lead to more severe capacity degradation.

The formation of a CEI layer at the cathode surface is confirmed by XPS analyses. The composition of the CEI includes (in)organic Li salts (LiF, LiCOOR), metal fluoride compounds (*i.e.* NiF$_2$), *etc*. The Li salts are believed to be formed from electrolyte oxidation and LiPF$_6$ decomposition. The formation of metal fluoride compounds is initiated by the transition metal dissolution process, which is driven by HF present in the electrolyte. Two possible mechanisms (Fig. 8 **A** and **B**) are involved in the cathode dissolution process. Mechanism represented by Fig. 8**A** can be described by Eq. 9, leading to products of NiF$_2$ and H$_2$O. Mechanism shown in Fig. 8**B** has been described by Eq. 10, leading to free Ni^{2+} ions, LiF and H$_2$O. The residual water is considered to be the origins of HF. Since water can be regenerated during metal dissolution, it therefore plays a role as a catalyst in the cathode dissolution process.

Conclusions

The ageing mechanisms of C_6/LiNi$_{0.5}$Mn$_{0.3}$Co$_{0.2}$O$_2$ batteries have been systematically investigated under various discharging currents and temperatures by means of electrochemical measurements and post-mortem analyses. The irreversible capacity losses (ΔQ_{ir}) which are calculated on the basis of the regularly determined EMF curves have been discussed. Two obvious degradation regions, denoted as L- and E-region, are observed in the ΔQ_{ir} curves at 30°C while only the L-region is observed at 60°C. This latter region is most likely anode-related and includes SEI formation, graphite electrode degradation, *etc*. The E-region can be related to the electrode degradation and battery polarization increase. The influence of discharging current on ΔQ_{ir} is determined by two independent parameters, time and cycle number. In the L-region, ΔQ_{ir} increases with increasing discharge current while ΔQ_{ir} decreases with increasing discharging current.

A non-destructive method based on the EMF derivative analyses has been applied to identify the degradation mechanisms of the individual electrodes. It has been concluded that the graphite degradation can be quantified with the evolution of plateau II from the dV_{EMF}/dQ *vs* Q_{out} plots while more voltage information can be obtained from the dV_{EMF}/dQ *vs* V plots.

Both the SEI formation at the anode and anode degradation have been experimentally confirmed by XPS analyses. The thickness of the SEI layers as well as their compositions are characterized by XPS depth-profiling measurements. Both Ni and Mn elements are detected at the anode while Co is absent, indicating that the bonding of Co in the cathode electrode is highly stable. A CEI layer is also detected at the cathode surface. The composition of the CEI layer includes Li salts, such as LiF, LiCOOR, as well as transition metal compounds, such as NiF_2. The NiF_2 detected at the cathode and the Ni element detected at the anode are attributed to the cathode dissolution processes. Cathode dissolution is considered to be driven by HF in the electrolyte, which originates from residual H_2O in the electrolyte.

Acknowledgements

References

[1] D.J. Li, H. Li, D. Danilov, L. Gao, J. Zhou, R.A. Eichel, Y. Yang, P.H.L. Notten, J Power Sources, 396 (2018) 444-452.
[2] B.J. Hwang, Y.W. Tsai, D. Carlier, G. Ceder, Chem Mater, 15 (2003) 3676-3682.
[3] Y. Koyama, I. Tanaka, H. Adachi, Y. Makimura, T. Ohzuku, J Power Sources, 119 (2003) 644-648.
[4] J. Choi, A. Manthiram, J Electrochem Soc, 152 (2005) A1714-A1718.
[5] R. Robert, C. Villevieille, P. Novak, J Mater Chem A, 2 (2014) 8589-8598.
[6] H. Bryngelsson, M. Stjerndahl, T. Gustafsson, K. Edström, Journal of Power Sources, 174 (2007) 970-975.
[7] D. Mohanty, H. Gabrisch, J Power Sources, 220 (2012) 405-412.
[8] D.A. Stevens, R.Y. Ying, R. Fathi, J.N. Reimers, J.E. Harlow, J.R. Dahn, Journal of the Electrochemical Society, 161 (2014) A1364-A1370.
[9] B. Stiaszny, J.C. Ziegler, E.E. Krauss, J.P. Schmidt, E. Ivers-Tiffee, J Power Sources, 251 (2014) 439-450.
[10] B. Stiaszny, J.C. Ziegler, E.E. Krauss, M.J. Zhang, J.P. Schmidt, E. Ivers-Tiffee, J Power Sources, 258 (2014) 61-75.
[11] Y. Kobayashi, T. Kobayashi, K. Shono, Y. Ohno, Y. Mita, H. Miyashiro, J Electrochem Soc, 160 (2013) A1181-A1186.
[12] Y. Kobayashi, T. Kobayashi, K. Shono, Y. Ohno, Y. Mita, H. Miyashiro, J Electrochem Soc, 160 (2013) A1415-A1420.
[13] Y. Li, M. Bettge, B. Polzin, Y. Zhu, M. Balasubramanian, D.P. Abraham, Journal of the Electrochemical Society, 160 (2013) A3006-A3019.
[14] V.A. Sethuraman, L.J. Hardwick, V. Srinivasan, R. Kostecki, J Power Sources, 195 (2010) 3655-3660.

[15] D.J. Li, D.L. Danilov, L. Gao, Y. Yang, P.H.L. Notten, J Electrochem Soc, 163 (2016) A3016-A3021.

[16] D.J. Li, D.L. Danilov, L. Gao, Y. Yang, P.H.L. Notten, Electrochim Acta, 210 (2016) 445-455.

[17] D.J. Li, D.L. Danilov, J. Xie, L. Raijmakers, L. Gao, Y. Yang, P.H.L. Notten, Electrochim Acta, 190 (2016) 1124-1133.

[18] Y. Qi, H.B. Guo, L.G. Hector, A. Timmons, J Electrochem Soc, 157 (2010) A558-A566.

[19] R. Deshpande, Y.T. Cheng, M.W. Verbrugge, J Power Sources, 195 (2010) 5081-5088.

[20] K. Amine, Z.H. Chen, Z. Zhang, J. Liu, W.Q. Lu, Y. Qin, J. Lu, L. Curtis, Y.K. Sun, J Mater Chem, 21 (2011) 17754-17759.

[21] D. Aurbach, B. Markovsky, G. Salitra, E. Markevich, Y. Talyossef, M. Koltypin, L. Nazar, B. Ellis, D. Kovacheva, J Power Sources, 165 (2007) 491-499.

[22] S.K. Jung, H. Gwon, J. Hong, K.Y. Park, D.H. Seo, H. Kim, J. Hyun, W. Yang, K. Kang, Adv Energy Mater, 4 (2014).

[23] H. Gabrisch, R. Yazami, Electrochem Solid St, 13 (2010) A88-A90.

[24] A. Tulsyan, Y. Tsai, R.B. Gopaluni, R.D. Braatz, Journal of Power Sources, 331 (2016) 208-223.

[25] Y.B. He, F. Ning, Q.H. Yang, Q.S. Song, B.H. Li, F.Y. Su, H.D. Du, Z.Y. Tang, F.Y. Kang, J Power Sources, 196 (2011) 10322-10327.

[26] V.-H. Duong, H.A. Bastawrous, K. Lim, K.W. See, P. Zhang, S.X. Dou, Journal of Power Sources, 296 (2015) 215-224.

[27] D. Danilov, R.A.H. Niessen, P.H.L. Notten, J Electrochem Soc, 158 (2011) A215-A222.

[28] V. Pop, H.J. Bergveld, J.H.G. Op het Veld, P.P.L. Regtien, D. Danilov, P.H.L. Notten, J Electrochem Soc, 153 (2006) A2013-A2022.

[29] M.S. Rad, D.L. Danilov, M. Baghalha, M. Kazemeini, P.H.L. Notten, Electrochim Acta, 102 (2013) 183-195.

[30] D. Li, in: Chemical Engineering and Chemistry, Eindhoven University of Technology, Eindhoven, 2017.

[31] R.I.R. Blyth, H. Buqa, F.P. Netzer, M.G. Ramsey, J.O. Besenhard, P. Golob, M. Winter, Appl Surf Sci, 167 (2000) 99-106.

[32] H.W. Nesbitt, D. Legrand, G.M. Bancroft, Phys Chem Miner, 27 (2000) 357-366.

[33] A.F. Carley, S.D. Jackson, J.N. O'Shea, M.W. Roberts, Surf Sci, 440 (1999) L868-L874.

[34] B.P. Lochel, H.H. Strehblow, J Electrochem Soc, 131 (1984) 713-723.

[35] M.W. Roberts, R.S. Smart, J Chem Soc Farad T 1, 80 (1984) 2957-2968.

[36] A.P. Grosvenor, M.C. Biesinger, R.S. Smart, N.S. McIntyre, Surf Sci, 600 (2006) 1771-1779.

[37] J.R. He, Y.F. Chen, P.J. Li, Z.G. Wang, F. Qi, J.B. Liu, Rsc Adv, 4 (2014) 2568-2572.

[38] X.K. Yang, D. Wang, R.Z. Yu, Y.S. Bai, H.B. Shu, L. Ge, H.P. Guo, Q.L. Wei, L. Liu, X.Y. Wang, J Mater Chem A, 2 (2014) 3899-3911.

[39] J. Meng, S.C. Zhang, X. Wei, P.H. Yang, S.B. Wang, J. Wang, H.L. Li, Y.L. Xing, G.R. Liu, Rsc Adv, 5 (2015) 81565-81572.

[40] W.J. Hao, H.H. Zhan, H. Chen, Y.H. Wang, Q.Q. Tan, F.B. Su, Particuology, 15 (2014) 18-26.

[41] J. Wang, Y.Y. Yu, B. Li, T. Fu, D.Q. Xie, J.J. Cai, J.B. Zhao, Phys Chem Chem Phys, 17 (2015) 32033-32043.

[42] Q. Li, G.S. Li, C.C. Fu, D. Luo, J.M. Fan, D.J. Xie, L.P. Li, J Mater Chem A, 3 (2015) 10592-10602.

[43] Z. Chen, J. Wang, D.L. Chao, T. Baikie, L.Y. Bai, S. Chen, Y.L. Zhao, T.C. Sum, J.Y. Lin, Z.X. Shen, Sci Rep-Uk, 6 (2016).

[44] D. McNulty, H. Geaney, C. O'Dwyer, Sci Rep-Uk, 7 (2017).

[45] Z.M. Luo, Y.G. Sun, H.Y. Liu, Chinese Chem Lett, 26 (2015) 1403-1408.

[46] A.N. Mansour, D.G. Kwabi, R.A. Quinlan, Y.C. Lu, S.H. Yang, J Electrochem Soc, 163 (2016) A2911-A2918.

[47] J.H. Park, J. Lim, J. Yoon, K.S. Park, J. Gim, J. Song, H. Park, D. Im, M. Park, D. Ahn, Y. Paik, J. Kim, Dalton T, 41 (2012) 3053-3059.

[48] A. Davidson, J.F. Tempere, M. Che, H. Roulet, G. Dufour, J Phys Chem-Us, 100 (1996) 4919-4929.

[49] S. Uhlenbrock, C. Scharfschwerdt, M. Neumann, G. Illing, H.J. Freund, J Phys-Condens Mat, 4 (1992) 7973-7978.

[50] B. Lochel, H.H. Strehblow, M. Sakashita, J Electrochem Soc, 131 (1984) 522-529.

[51] W.L. Guo, Y.F. E, L. Gao, L.Z. Fan, S.H. Yang, Chem Commun, 46 (2010) 1290-1292.

[52] L. Daheron, H. Martinez, R. Dedryvere, I. Baraille, M. Menetrier, C. Denage, C. Delmas, D. Gonbeau, J Phys Chem C, 113 (2009) 5843-5852.

[53] C.H. Ding, D. Yan, Y.J. Zhao, Y.Z. Zhao, H.P. Zhou, J.B. Lia, H.B. Jin, Phys Chem Chem Phys, 18 (2016) 25879-25886.

[54] D. Li, H. Li, D. Danilov, L. Gao, J. Zhou, R.-A. Eichel, Y. Yang, P.H.L. Notten, J Power Sources, 396 (2018) 444-452.

[55] D. Li, D. Danilov, B. Zwikirsch, M. Fichtner, Y. Yang, R.-A. Eichel, P.H.L. Notten, J Power Sources, (2018) 106-117.

[56] D.J. Li, D. Danilov, Z.R. Zhang, H.X. Chen, Y. Yang, P.H.L. Notten, J Electrochem Soc, 162 (2015) A858-A869.

[57] D. Li, D. Danilov, Z. Zhang, H. Chen, Y. Yang, P.H.L. Notten, ECS Transactions, 62 (2014) 8.

[58] W. Choi, A. Manthiram, J Electrochem Soc, 153 (2006) A1760-A1764.

[59] A. Gennaro, A.A. Isse, J.M. Saveant, M.G. Severin, E. Vianello, J Am Chem Soc, 118 (1996) 7190-7196.